International Journal of Mass Spectrometry 441 (2019) 32–43

Contents lists available at ScienceDirect

International Journal of Mass Spectrometry

journal homepage: www.elsevier.com/locate/ijms

Full Length Article

IRMPD action spectroscopy, ER-CID experiments, and theoretical approaches investigate intrinsic L-thymidine properties compared to D-thymidine: Findings support robust methodology

Erik O. Soley[a], Zachary J. Devereaux[a], L.A. Hamlow[a], G. Berden[b], J. Oomens[b], M.T. Rodgers[a,*]

[a] Wayne State University, Department of Chemistry, 5101 Cass Avenue, Detroit, MI, 48202, United States
[b] Radboud University, Institute for Molecules and Materials, FELIX Laboratory, Toernooiveld 7c, 6525 ED, Nijmegen, the Netherlands

ARTICLE INFO

Article history:
Received 9 January 2019
Received in revised form 4 April 2019
Accepted 5 April 2019
Available online 6 April 2019

Keywords:
L-Thymidine
Telbivudine
Thymidine
Enantiomers
Infrared multiple photon dissociation (IRMPD) action spectroscopy
Energy-resolved collision-induced dissociation (ER-CID)

ABSTRACT

L-Thymidine (L-dThd) is the enantiomer of D-thymidine (dThd), a naturally-occurring pyrimidine nucleoside found within DNA nucleic acids. L-dThd, also known as Telbivudine, does not occur naturally, but in the last decade has found successful application as an antiviral medication for hepatitis B virus infection. In this work, the gas-phase conformers of the protonated and sodium cationized forms of L-dThd, $[L\text{-dThd+H}]^+$ and $[L\text{-dThd + Na}]^+$, are investigated using infrared multiple photon dissociation (IRMPD) action spectroscopy complemented by electronic structure calculations performed at the B3LYP/6-311+G(2d,2p)//B3LYP/6-311+G(d,p) level of theory. Comparisons between the experimental IRMPD spectra and theoretical linear IR spectra elucidate the stable low-energy conformations adopted by these L-dThd complexes generated by electrospray ionization. Minor 2,4-dihydroxy tautomers (T) and O2 protonated conformers contribute to the experimental $[L\text{-dThd+H}]^+$ population, whereas conformers involving tridentate binding of Na^+ to the O2, O4′, and O5′ atoms primarily contribute to the experimental $[L\text{-dThd + Na}]^+$ population. Theory predicts a tautomer as the protonated ground conformer of $[L\text{-dThd+H}]^+$ with thymine in an *anti* orientation and a tridentate (O2O4′O5′) sodium cationized ground conformer with a *syn* thymine orientation, consistent with theoretical predictions for $[d\text{Thd+H}]^+$ and $[d\text{Thd + Na}]^+$, respectively. Both protonated and sodium cationized L-dThd and dThd illustrate highly parallel IRMPD spectral features as expected. Survival yield analyses of data from energy-resolved collision-induced dissociation experiments elucidate the relative stabilities of $[L\text{-dThd+H}]^+$ and $[L\text{-dThd + Na}]^+$ as compared to the corresponding enantiomeric systems. Identical results are exhibited in the survival yield analyses as anticipated for enantiomeric complexes to simple cations. This work employs the same robust methodology that has provided structural characterization and energetic insight for similar systems preceding it to validate the parallel theoretical and experimental behaviors expected for enantiomers.

1. Introduction

Nucleosides are the fundamental components of nucleic acids, both DNA and RNA, which define the cellular code of life. The various intracellular mechanisms employed upon this code allow for its regular replication to occur in new cell growth and the transfer of genetic information during reproduction to foster stable continuation of life. When viral infection occurs, these intracellular mechanisms are hijacked by the attacking virus and used for the purpose of generating new copies of the virus to propagate the infection process. There are many types of viruses that replicate using different methods. Viruses with a DNA genome use

Abbreviations: FELIX, free electron laser for infrared experiments; L-dThd, L-Thymidine; dThd, D-Thymidine; IRMPD, infrared multiple photon dissociation; ER-CID, energy-resolved collision-induced dissociation; HBV, hepatitis B virus; HIV, human immunodeficiency virus; ETD, electron transfer dissociation; QIT MS, quadrupole ion trap mass spectrometer; FT-ICR MS, Fourier transform ion cyclotron resonance mass spectrometer; ESI, electrospray ionization; OPO/OPA, optical parametric oscillator/amplifier; SWIFT, stored waveform inverse Fourier transform; DFT, density functional theory; FWHM, full-width-at-half-maximum; IVR, intramolecular vibrational redistribution; FEL, free electron laser.

* Corresponding author at: 5101 Cass Avenue, Detroit, MI, 48202, United States.
E-mail address: mrodgers@chem.wayne.edu (M.T. Rodgers).

https://doi.org/10.1016/j.ijms.2019.04.003
1387-3806/

the nucleus of the host cell and enzymes to replicate viral DNA and assemble new viruses with cellular mechanisms [1], whereas retroviruses with an RNA genome use viral reverse transcriptase to reverse transcribe its RNA into a linear DNA duplex to integrate within the host cell genome to make new viruses [2]. Hepatitis B virus (HBV) is a DNA virus that exhibits unique characteristics similar to retroviruses by replicating through an RNA intermediate that is reverse transcribed into viral DNA that subsequently becomes incorporated into the host cell genome, causing the cellular mechanisms to produce new hepatitis B viruses [3–5]. These particular attributes of the HBV replication cycle allow the virus to remain elusive from human immune responses and persist in infected cells. HBV infection is known to progress to varying degrees of liver disease including acute and chronic inflammation of liver tissue, cirrhosis, and hepatocellular carcinoma [4–6]. In 2015 alone, nearly 260 million people worldwide were estimated to have chronic hepatitis B infection, and approximately one million people died from associated cirrhosis and liver cancer caused by the virus, a 22% increase in mortality since 2000 [7]. Without aggressive treatment intervention, these global figures are expected to rise.

Naturally and synthetically-modified nucleosides have proven to be effective antiviral and anticancer therapies for various diseases [8–15]. However, drug resistance has developed with many of these medications for the treatment of HBV, human immunodeficiency virus (HIV), and different types of cancer, prompting increased use of combination drug therapies to achieve effective patient outcomes [3,6,9,12,15]. While there are several antiviral nucleoside drugs that remain effective when used alone in targeted treatment with little resistance, cytotoxicity, or other noted side effects [6,9,10], an urgency for future drug design to combat these ever-evolving viruses still remains. Previously it was believed that only the D-nucleoside analogues that exhibited the same configuration as their natural counterparts would be biologically active with stereospecific enzymes [16]. When this rigid lock-and-key approach was discovered to be more flexible than originally theorized, the respective L-nucleoside enantiomers (non-superimposable mirror images of the D-nucleosides) were investigated for antiviral attributes with rewarding results. Thus far, 13 antiviral drugs have been developed for antiviral treatment modalities using D-nucleosides as the fundamental components for drug design approaches [17]. One of those drugs, L-thymidine (L-dThd), also known in the medical community by the name Telbivudine, is the L-enantiomer of naturally occurring D-thymidine (dThd). L-dThd has illustrated successful HBV treatment outcomes compared to similar drugs [17–23]. Further studies involving L-nucleosides and their variants may provide crucial insight into future drug design approaches and targeted therapies involving stereospecific natural mechanisms.

Previous studies involving dThd employed theoretical computational and tandem mass spectrometry approaches to investigate various intrinsic properties of the protonated and sodium cationized forms of the nucleoside [24–26]. These included relative nucleoside stability and N-glycosidic bond stability using energy-resolved collision-induced dissociation (ER-CID), the stable conformations adopted in the gas phase by comparing measured infrared multiple photon dissociation (IRMPD) spectra with linear IR spectra predicted for stable low-energy structures, the ER-CID versus IRMPD fragmentation pathways, and the effects of protonation versus sodium cationization upon the energetics and gas-phase conformations adopted in the experiments. These approaches have proven effective for structural characterization and energetic studies of other nucleosides [24–40]. This study investigates L-dThd using parallel methodologies. Because enantiomers exhibit the same physical properties and only differ in their connectivity of atoms in space and rotation of plane-polarized light, their interactions with simple cations are expected to produce theoretical and experimental results that are identical. Thus, the theoretical and experimental results for L-dThd are compared to those of dThd to assess the robustness of the methodologies employed.

2. Experimental and theoretical methods

2.1. Instrumentation, materials, and sample preparation

ER-CID experiments were performed using a Bruker amaZon ETD quadrupole ion trap mass spectrometer (QIT MS, Bruker Daltonics, Bremen, Germany) at Wayne State University. L-dThd (Carbosynth, San Diego, CA, USA) and dThd (Sigma-Aldrich, St. Louis, MO, USA) were dissolved to concentrations of ~10 and ~25 μM in 50/50 (v/v) HPLC grade methanol and water (Sigma-Aldrich, St. Louis, MO, USA) in 2 mL plastic microcentrifuge tubes (Light Labs, Dallas, TX, USA). $[L\text{-dThd+H}]^+$ and $[dThd+H]^+$ were generated from ~25 μM solutions of the nucleosides modified with ~1% (v/v) acetic acid (Mallinckrodt Chemicals, Phillipsburg, NJ, USA). $[L\text{-dThd} + Na]^+$ and $[dThd + Na]^+$ were generated from ~10 μM solutions modified with 5 μM sodium acetate (EMD, Gibbstown, NJ, USA).

IRMPD action spectroscopy experiments were performed using a custom 4.7 T Fourier transform ion cyclotron resonance mass spectrometer (FT-ICR MS) at the Free Electron Laser for Infrared eXperiments (FELIX) Laboratory at Radboud University Nijmegen in The Netherlands. L-dThd and dThd were dissolved to a concentration of ~1 mM in 50/50 (v/v) HPLC grade methanol and water (Sigma-Aldrich, Zwijndrecht, The Netherlands) in 2 mL plastic microcentrifuge tubes (Fisher Scientific, Landsmeer, The Netherlands). $[L\text{-dThd+H}]^+$ and $[dThd+H]^+$ were generated from solutions of the nucleosides containing ~1% (v/v) acetic acid (Sigma-Aldrich, Zwijndrecht, The Netherlands). $[L\text{-dThd} + Na]^+$ and $[dThd + Na]^+$ were generated from solutions containing ~0.5 mM sodium acetate (Sigma-Aldrich, Zwijndrecht, The Netherlands).

2.2. QIT MS and ER-CID

ER-CID experiments of $[L\text{-dThd+H}]^+$, $[L\text{-dThd} + Na]^+$, $[dThd+H]^+$, and $[dThd + Na]^+$ were performed herein using a QIT MS. ER-CID experiments of $[dThd+H]^+$ and $[dThd + Na]^+$ were also previously performed and published relative to parallel forms of 5-methyluridine $[Thd+H]^+$ and $[Thd + Na]^+$ [25]. L-dThd and dThd sample solutions were introduced to the atmospheric pressure Apollo II ESI source at a flow rate of 3 μL/min to generate the respective precursor ions. Helium, maintained near ~1 mTorr stagnation pressure in the QIT chamber, served as the neutral collision gas for the ER-CID experiments. The low-mass cutoff was set to 27% of the precursor ion *m/z*. The rf excitation amplitude (rf_{EA}) is applied to the end cap electrodes of the ion trap and gradually ramped in 0.01 V increments from 0.00 V to beyond the rf_{EA} necessary for complete precursor ion dissociation. The rf_{EA} was applied for 100 ms in each mass analysis sequence. The total mass spectra collection time per rf_{EA} step was 30 s. Experiments were performed in triplicate to assess reproducibility. Data analysis of the ion chromatograms and mass spectra were performed using Compass Data Analysis Software 4.0 (Bruker Daltonics, Bremen, Germany).

2.3. Survival yield analysis

With judicial execution of ER-CID experiments, survival yield analysis provides a robust method to elucidate relative precursor ion stabilities [25,31–36,41–48]. Survival yields were calculated using Eq. (1) as a function of rf_{EA} for $[L\text{-dThd+H}]^+$, $[dThd+H]^+$,

$[\text{L-dThd} + \text{Na}]^+$, and $[\text{dThd} + \text{Na}]^+$ using the mass spectral data acquired in the ER-CID experiments.

$$\text{Survival} \quad \text{Yield} = I_p/(I_p + \Sigma_i I_{f_i}) \tag{1}$$

where I_p is the precursor ion intensity, I_{fi} is the ion intensity of fragment ion i, such that $(I_p + \Sigma_i I_{f_i})$ is the total ion intensity. Survival yields were calculated using custom software developed in our laboratory. Survival yields were plotted as a function of rf_{EA}, and each data set was least-squared fit with the four-parameter logistic curve given in Eq. (2).

$$\text{Survival} \quad \text{Yield} = min + \frac{max - min}{1 + (rf_{EA}/CID_{50\%})^{CIDslope}} \tag{2}$$

In this equation, *min* and *max* represent the minimum (0) and maximum (1) values of the survival yield, and *CIDslope* is the slope of the decreasing region of the survival yield curve. The rf_{EA} required to produce 50% precursor ion dissociation ($CID_{50\%}$) is extracted from the fit and used to compare the relative stabilities of $[\text{L-dThd+H}]^+$, $[\text{dThd+H}]^+$, $[\text{L-dThd} + \text{Na}]^+$, and $[\text{dThd} + \text{Na}]^+$. Construction of survival yield curves and fits to the data were performed using SigmaPlot 10.0 (Systat Software, Inc., San Jose, CA, USA).

2.4. FT-ICR MS and photodissociation

IRMPD action spectroscopy experiments were performed on $[\text{L-dThd+H}]^+$ and $[\text{L-dThd} + \text{Na}]^+$ using a FT-ICR MS coupled to either the FELIX [49] beamline or an optical parametric oscillator/amplifier (OPO/OPA) infrared laser light source [49–52]. $[\text{L-dThd+H}]^+$ and $[\text{L-dThd} + \text{Na}]^+$ ions were generated by delivering the respective sample solutions to a Micromass "Z-spray" electrospray ionization (ESI) source at a flow rate of 5.0 μL/min. The ions were accumulated in an rf hexapole ion trap for several seconds to promote ion cooling prior to being pulse extracted through a quadrupole ion bender and subsequently introduced into the FT-ICR cell through a 1 m long rf octopole ion guide [50]. A pulsed DC bias voltage switch is applied along the octopole to allow ion capturing with minimal collisional heating of the ions. After introduction into the ICR cell, the ions were trapped for ~300 ms to promote radiative emission of any excess internal energy. $[\text{L-dThd+H}]^+$ and $[\text{L-dThd} + \text{Na}]^+$ precursor ions were mass isolated using stored waveform inverse Fourier transform (SWIFT) techniques. The mass isolated precursor ions were irradiated with infrared laser light to promote photodissociation of the selected ions. The ions were irradiated for 0.5–1 s by the free electron laser in the IR fingerprint region from ~500–1850 cm^{-1}, and for 9 s by the OPO/OPA laser in the hydrogen-stretching region from ~3300–3800 cm^{-1}. IRMPD yields were calculated as a function of wavelength (or vibrational frequency) using Eq. (3).

$$\text{IRMPD Yield} = \sum\nolimits_i I_{f_i} \;/\; (I_p + \sum\nolimits_i I_{f_i}) \tag{3}$$

where I_p and I_{fi} are as described in Eq. (1). Experimental IRMPD yields were linearly corrected with laser power calibration curves (see **Fig. S1**) to partially account for the effects of variation in the laser power across the frequency ranges investigated.

2.5. Computational details

The chemical structures and atom numbering of neutral dThd and L-dThd are shown in Fig. 1. $[\text{L-dThd+H}]^+$ and $[\text{L-dThd} + \text{Na}]^+$ calculations were performed in this work, whereas results for $[\text{dThd+H}]^+$ and $[\text{dThd} + \text{Na}]^+$ were previously reported and used for comparisons here [24,25]. Parallel computational methods were used here to ensure meaningful comparisons. The potentially favorable L-dThd protonation states that were constructed included O2

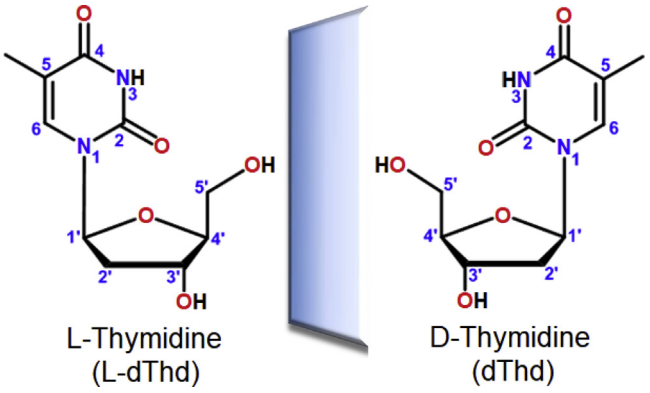

Fig. 1. Chemical structures of L-thymidine (L-dThd) and D-thymidine (dThd) illustrating non-superimposable characteristics of the enantiomers. Numbering of the thymine nucleobase and sugar moieties is shown.

protonation, O4 protonation, and a 2,4-dihydroxy tautomer. The sodium cationized L-dThd structures that were constructed initially involved monodentate O2, O4, N3, O3′, O4′, and O5′ interactions with Na^+. Candidate structures were generated from each of these initial constructs by a simulated annealing procedure using HyperChem software [53] with the Amber 3 force field. The simulated annealing process involved 300 cycles of annealing, with each cycle beginning at 0 K, heating to 1000 K over 0.3 ps, maintaining 1000 K for 0.2 ps to sample conformational space, and cooling back to 0 K over 0.3 ps. The Amber 3 force field optimized the resulting structure to a local minimum, this candidate structure was captured as a snapshot, and the structure was used as the initial structure in the subsequent annealing cycle. After simulated annealing, ~10% of the resulting candidate conformers were chosen, based primarily upon their relative stabilities, for higher level optimization. Over 500 protonated and sodium cationized L-dThd snapshot structures from the simulated annealing procedure were selected for density functional theory (DFT) calculations using the Gaussian 09 suite of programs [54]. Geometry optimizations and frequency analyses were performed at the B3LYP/6-311+G(d,p) level of theory at 298.15 K and 1 bar with a frequency scaling factor of 0.9887 [55]. Single point energies were calculated at the B3LYP/6-311+G(2d,2p) level of theory. In the IR fingerprint region, the $[\text{L-dThd+H}]^+$ and $[\text{L-dThd} + \text{Na}]^+$ vibrational frequencies were scaled by factors of 0.9840 and 0.9785, respectively. In the hydrogen-stretching region, the $[\text{L-dThd+H}]^+$ and $[\text{L-dThd} + \text{Na}]^+$ vibrational frequencies were scaled by factors of 0.9525 and 0.9545, respectively. Different scale factors were used to better approximate experimental variations encountered between systems and provide a more accurate spectral alignment between experimental and theoretical results in both regions of the IR spectrum. All vibrations are considered when deciding appropriate scaling factors for alignment of the predicted IR spectra with the experimental spectra, with particular emphasis given to aligning with the most intense peaks in the experimental spectra. In order to facilitate comparisons with the experimental IRMPD spectra and partially account for the room temperature distribution of the ions, the laser bandwidth, and the effects of anharmonicity of the resonant vibrational modes, the calculated vibrational frequencies were broadened using a 25 cm^{-1} full-width-at-half-maximum (FWHM) Gaussian line shape over the fingerprint region for both $[\text{L-dThd+H}]^+$ and $[\text{L-dThd} + \text{Na}]^+$, and in the hydrogen-stretching region a 25 cm^{-1} FWHM Gaussian line shape was used for $[\text{L-dThd+H}]^+$, whereas a 15 cm^{-1} FWHM Gaussian line shape was used for $[\text{L-dThd} + \text{Na}]^+$. Unique stable conformers of $[\text{L-dThd+H}]^+$ and $[\text{L-dThd} + \text{Na}]^+$ were selected based upon the relative Gibbs energies at 298 K and visual comparison with other conformers.

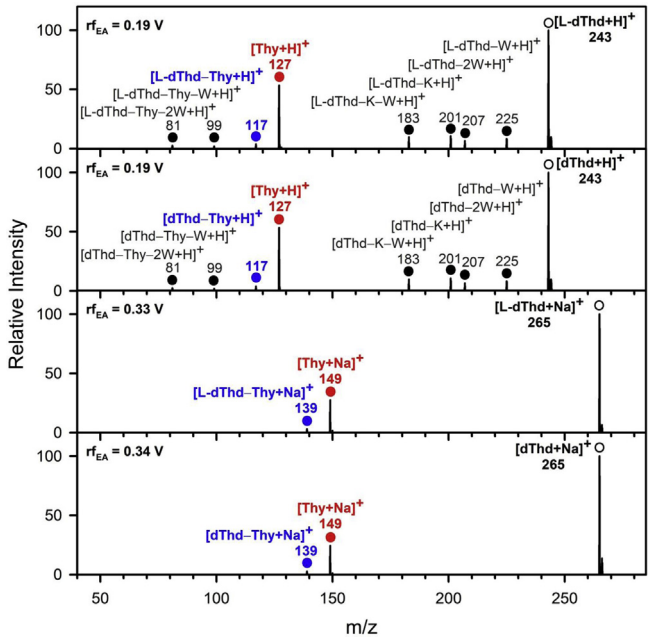

Fig. 2. CID mass spectra of $[L\text{-dThd+H}]^+$, $[dThd+H]^+$, $[L\text{-dThd} + Na]^+$, and $[dThd + Na]^+$ at rf excitation amplitudes that produce ~50% precursor ion dissociation. In each mass spectrum the precursor ions are indicated with open circles. The protonated/sodium cationized Thy nucleobase ions are indicated with solid red circles, and the protonated/sodium cationized 2′-deoxyribose sugar ions are indicated with solid blue circles, both of which result from glycosidic bond cleavage of their respective precursor ions (For interpretation of the references to colour in this figure legend, the reader is referred to the web version of this article).

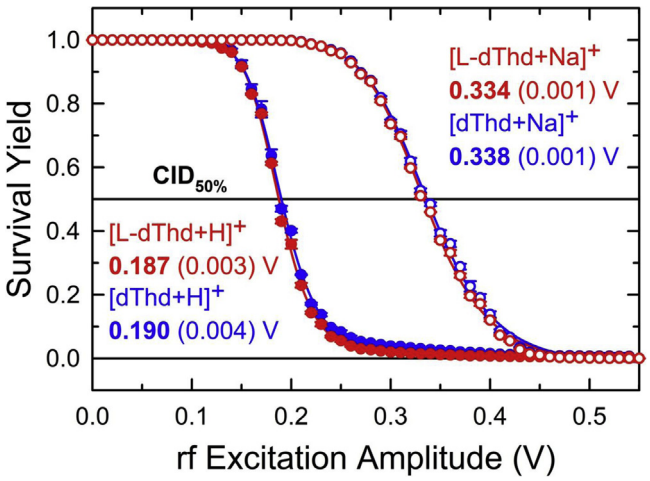

Fig. 3. Survival yield curves of $[L\text{-dThd+H}]^+$, $[dThd+H]^+$, $[L\text{-dThd} + Na]^+$, and $[dThd + Na]^+$. Data for the protonated nucleosides are indicated with solid symbols, whereas results for the sodium cationized nucleosides are indicated with open symbols. The L-dThd species are shown in red, whereas the D-dThd species are shown in blue. The $CID_{50\%}$ values along with uncertainties (reported as one standard deviation) extracted from least squares fitting to Eq. (2) are also shown (For interpretation of the references to colour in this figure legend, the reader is referred to the web version of this article).

3. Results

3.1. QIT MS ER-CID

CID mass spectra of $[L\text{-dThd+H}]^+$, $[dThd+H]^+$, $[L\text{-dThd} + Na]^+$, and $[dThd + Na]^+$ acquired at an rf_{EA} that produces ~50% precursor ion dissociation are compared in Fig. 2. As expected for enantiomers, the CID behavior is highly parallel and rf excitation amplitudes at $CID_{50\%}$ are equal to within experimental error for $[L\text{-dThd+H}]^+$ and $[dThd+H]^+$ ($rf_{EA} = 0.19$ V) as well as for $[L\text{-dThd} + Na]^+$ and $[dThd + Na]^+$ ($rf_{EA} = 0.33$ V and $rf_{EA} = 0.34$ V, respectively). The parallel fragmentation behavior observed for the enantiomer pairs is further illustrated in Fig. 3 where the ER-CID survival yield curves are shown. The mass spectra at $CID_{50\%}$ for the protonated and sodium cationized nucleosides illustrate nearly perfect agreement with the fragment ions and their respective intensities. The dominant fragmentation pathways for all four species involves N-glycosidic bond cleavage as depicted in **Reactions 4** and **5**,

$$[L/D\text{-dThd+Cation}]^+ \xrightarrow{n\,He} [Thy+Cation]^+ + (L/D\text{-dThd–Thy}) \quad (4)$$

$$[L/D\text{-dThd+Cation}]^+ \xrightarrow{n\,He} [L/D\text{-dThd–Thy+Cation}]^+ + Thy \quad (5)$$

where L/D-dThd represent L-dThd and D-dThd, respectively, Cation = H^+ or Na^+, and Thy is the thymine nucleobase. **Reactions 4** and **5** are the only CID fragmentation pathways observed for both $[L\text{-dThd} + Na]^+$ and $[dThd + Na]^+$ in the QIT MS. Previous combined guided ion beam tandem mass spectrometry and theoretical studies of the glycosidic bond cleavage reactions of $[dThd+H]^+$ as well as other protonated nucleosides suggest that the protonated nucleobase (**Reaction 4**) is produced by lengthening/cleavage of the glycosidic bond followed by transfer of the H2′ proton from the sugar to the nucleobase, whereas the protonated sugar is produced by elimination of the neutral nucleobase (**Reaction 5**) via simple lengthening/cleavage of the glycosidic bond [56,57]. Somewhat parallel glycosidic bond cleavage mechanisms are anticipated for the sodium cationized nucleosides, but have yet to be explored. As can be seen in all four mass spectra, **Reaction 4** is more favorable than **Reaction 5** as the [Thy + Cation]$^+$ ion intensities are significantly greater than those of [L/D-dThd–Thy + Cation]$^+$. Both protonated nucleosides exhibit additional fragmentation pathways contributing to the greater variety of ions observed within the mass spectra. This is likely due to the relatively low stability of the protonated sugar moiety. **Reactions 6** and **7** illustrate two fragmentation pathways competitive with glycosidic bond cleavage, where ketene (K, $H_2C=C=O$) and water (W) losses are observed.

$$[L/D\text{-dThd+H}]^+ \xrightarrow{n\,He} [L/D\text{-dThd–K+H}]^+ + K \quad (6)$$

$$[L/D\text{-dThd+H}]^+ \xrightarrow{n\,He} [L/D\text{-dThd–K–W+H}]^+ + K + W \quad (7)$$

Several minor fragmentation pathways involving water and Thy nucleobase elimination are observed with both protonated nucleosides as well, described by **Reactions 8–11**.

$$[L/D\text{-dThd+H}]^+ \xrightarrow{n\,He} [L/D\text{-dThd–W+H}]^+ + W \quad (8)$$

$$[L/D\text{-dThd+H}]^+ \xrightarrow{n\,He} [L/D\text{-dThd–2W+H}]^+ + 2W \quad (9)$$

$$[L/D\text{-dThd+H}]^+ \xrightarrow{n\,He} [L/D\text{-dThd–Thy–W+H}]^+ + Thy + W \quad (10)$$

$$[L/D\text{-dThd+H}]^+ \xrightarrow{n\,He} [L/D\text{-dThd–Thy–2W+H}]^+ + Thy + 2W \quad (11)$$

The losses observed in **Reactions 7** and **9–11** all involve sequential processes. The results of **Reaction 7** are achieved via sequential loss of W or K from the ionic products of **Reaction 6** or **Reaction 8**, respectively. The ionic product of **Reaction 8** may undergo further dissociation such as neutral loss of an additional W, **Reaction 9**, or neutral loss of Thy, **Reaction 10**. The ionic product of **Reaction 10** may also be formed by neutral loss of W subsequent to **Reaction 4**. The ionic product of **Reaction 11** is formed by additional neutral loss of W following **Reaction 10**, but could also occur via glycosidic bond cleavage of the ionic product of **Reaction 9**. The proposed CID reaction pathways for $[L/D\text{-dThd+H}]^+$ are also schematically summarized in **Fig. S2**.

3.2. IRMPD action spectroscopy

IR irradiation of $[L\text{-dThd+H}]^+$ and $[L\text{-dThd + Na}]^+$ resulted in several photodissociation pathways being observed as described in **Reactions 12–14**,

$$[\text{L-dThd+Cation}]^+ \overset{n\,h\nu}{\rightarrow} [\text{Thy+Cation}]^+ + (\text{L-dThd–Thy}) \quad (12)$$

$$[\text{L-dThd+Cation}]^+ \overset{n\,h\nu}{\rightarrow} [\text{L-dThd–Thy+Cation}]^+ + \text{Thy} \quad (13)$$

$$[\text{L-dThd+Cation}]^+ \overset{n\,h\nu}{\rightarrow} [\text{Cation}]^+ + \text{L-dThd} \quad (14)$$

as before, Cation = H^+ or Na^+ and Thy is the thymine nucleobase. With both the FELIX and OPO/OPA excitation sources, the IR photodissociation pathways remained unchanged for each system. Only **Reaction 12** was observed for $[L\text{-dThd+H}]^+$, corresponding to N-glycosidic bond cleavage with the excess proton retained by the Thy nucleobase with concomitant neutral sugar loss. **Reactions 12–14** were all observed for $[L\text{-dThd + Na}]^+$. **Reactions 12** and **13** involve N-glycosidic bond cleavage and are exact analogues to **Reactions 4** and **5** discussed earlier (Section 3.1). A neutral sugar loss occurs with Na^+ retention by the Thy nucleobase in **Reaction 12**, whereas the opposite occurs in **Reaction 13** with loss of neutral Thy and retention of Na^+ by the sugar. **Reaction 14** corresponds to simple noncovalent dissociation of Na^+ from L-dThd; the analogous reaction likely occurs under CID conditions, but was not observed in the QIT MS due to the low-mass cutoff. This conclusion that **Reaction 14** occurs upon CID was confirmed by examining the CID behavior of $[L\text{-dThd + Na}]^+$ in the FT-ICR MS where detectable Na^+ was indeed observed. The experimental IRMPD spectra of $[L\text{-dThd+H}]^+$ and $[d\text{Thd+H}]^+$ are compared with $[L\text{-dThd + Na}]^+$ and $[d\text{Thd + Na}]^+$ in Fig. 4. As expected, highly parallel results are observed between the dThd and L-dThd enantiomers. The modest discrepancies observed between dThd and L-dThd systems with the same cationization agent likely result from slight differences in the experiments and data processing rather than from actual chemical differences between the enantiomers. The vast differences observed in the IRMPD spectra when the cationization agent is varied between protonation and sodium cationization clearly indicate distinct structural and chemical differences between these forms.

3.3. Nomenclature for designating stable conformations

Stable structures of the protonated L-dThd and dThd nucleosides are designated based on the site of protonation or tautomeric state followed by an uppercase letter in alphabetical order depicting the order of stability, from most stable to least stable, ranked according to the relative Gibbs energies at 298 K of the theoretical structures that exhibit the same protonation or tautomeric state. O2 and O4 designations correspond to protonation at the O2 and O4 atoms, respectively, whereas T designations correspond to 2,4-dihydroxy tautomers.

Sodium cationized theoretical stable structures are designated with a capital letter representing the type of chelation interactions between the Na^+ cation and L-dThd and dThd nucleoside (T for tridentate, B for bidentate, and M for monodentate). The number following the letter designation indicates the order of stability, from most stable to least stable, ranked according to the relative Gibbs energies at 298 K of the theoretical structures that exhibit the same type of cation binding modes. **Fig. S3** illustrates the structural designation methodology employed in this study as previously described [25,31–34,58]. This figure illustrates the two possible designations for the Thy nucleobase as well as the major and minor sugar puckering aspects.

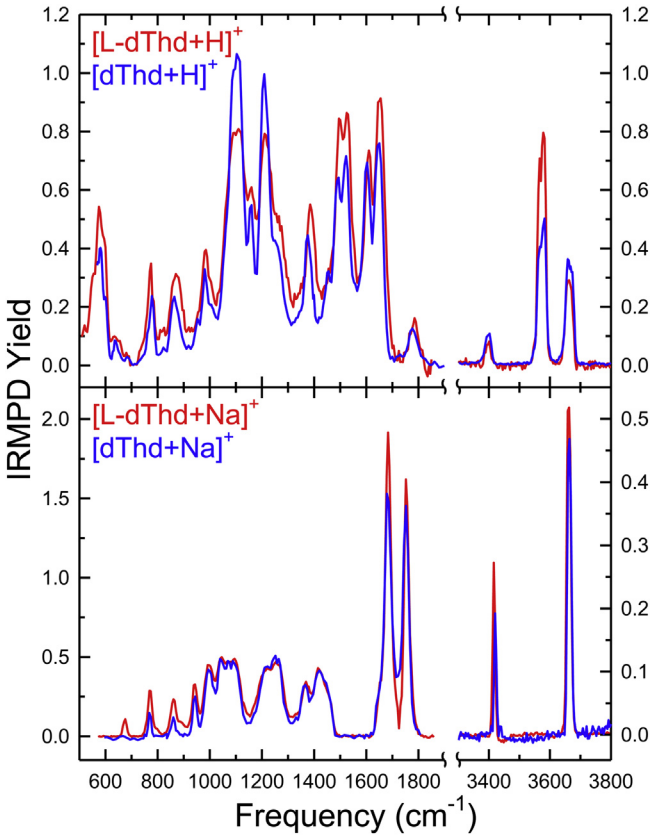

Fig. 4. Infrared multiple photon dissociation (IRMPD) action spectra of $[L\text{-dThd+H}]^+$, $[d\text{Thd+H}]^+$, $[L\text{-dThd + Na}]^+$, and $[d\text{Thd + Na}]^+$ in the IR fingerprint (500–1900 cm^{-1}) and hydrogen-stretching (3300–3800 cm^{-1}) regions; data for $[d\text{Thd+H}]^+$ and $[d\text{Thd + Na}]^+$ are taken from references [24] and [25].

3.4. Calculated conformations of $[L\text{-dThd+H}]^+$ and $[L\text{-dThd + Na}]^+$

The ground conformers of $[L\text{-dThd+H}]^+$ and $[L\text{-dThd + Na}]^+$ are nonsuperimposable mirror images to their ground enantiomer counterparts, $[d\text{Thd+H}]^+$ and $[d\text{Thd + Na}]^+$ [24,25]. (see Fig. 5) The enantiomer pairs exhibit the same cation binding mode, Thy nucleobase orientation, major and minor sugar puckering features, and relative Gibbs energies at 298 K. The high level of agreement for both the protonated and sodium cationized L-dThd and dThd ground conformers is further illustrated in Table 1, which lists geometric information for each optimized structure. Both $[L\text{-dThd+H}]^+$ and $[d\text{Thd+H}]^+$ ground conformers exhibit T tautomeric protonation states with *anti* Thy nucleobase orientations and C2′-endo ($^2T_3$) sugar puckering. Both $[L\text{-dThd + Na}]^+$ and $[d\text{Thd + Na}]^+$ ground conformers exhibit tridentate Na^+ binding to the O2, O4′, and O5′ atoms, forming a 5-membered chelation ring with the sugar moiety and a 6-membered chelation ring with the Thy nucleobase, with *syn* nucleobase orientations and O4′-endo ($^OT_1$) sugar puckering. As enantiomeric pairs, the high degree of parallelism among these systems was expected, and provides additional confirmation of the robustness of the theoretical methodology employed in this and our earlier related works [24,25,27–37].

Table 2 lists low-energy optimized conformers of $[L\text{-dThd+H}]^+$ and $[L\text{-dThd + Na}]^+$ with relevant energetic and geometric details. **Figs. S4** and **S5** show all unique stable structures calculated for $[L\text{-dThd+H}]^+$ and $[L\text{-dThd + Na}]^+$. Additional discussion regarding the stable conformations of $[L\text{-dThd+H}]^+$ and $[L\text{-dThd + Na}]^+$ as well as comparisons of low-energy conformers of protonated and sodium cationized dThd vs L-dThd is available in the Supplementary materials.

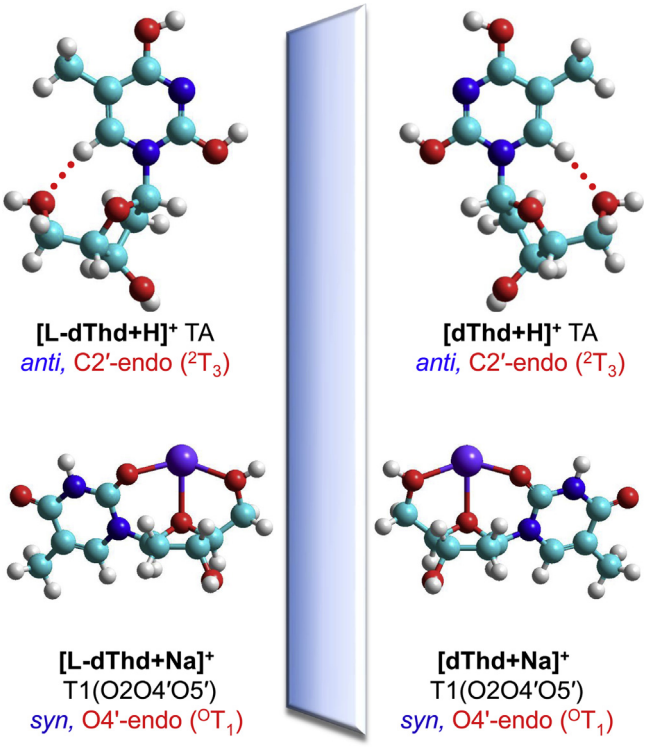

Fig. 5. Ground conformers of [L-dThd+H]$^+$ and [L-dThd + Na]$^+$ as predicted at the B3LYP/6-311+G(2d,2p)//B3LYP/6-311+G(d,p) level of theory at 298 K are shown with their respective cation binding mode, nucleobase orientation, and sugar puckering. The ground conformers of [dThd+H]$^+$ and [dThd + Na]$^+$ are presented for comparison and taken from references [24] and [25].

Table 1
Geometric Details of the B3LYP/6-311+G(d,p) Ground Conformers of the Protonated and Sodium Cationized Forms of the L- and D- Enantiomers of dThd.[a]

	[L-dThd+H]$^+$		[dThd+H]$^+$	
Conformer Designation	**TA**		**TA**	
Bond Length	H···O2	0.970 Å	H···O2	0.970 Å
	H···O4	0.971 Å	H···O4	0.971 Å
Glycosidic Bond Length	N1···C1′	1.512 Å	N1···C1′	1.511 Å
Bond Angle	∠HO2C2	109.2°	∠HO2C2	109.2°
	∠HO4C4	110.3°	∠HO4C4	110.3°
Dihedral Angle	∠C2N1C1′O4′	134.6°	∠C2N1C1′O4′	−134.6°
	∠O5′C5′C4′O4′	63.7°	∠O5′C5′C4′O4′	−63.6°
	[L-dThd+Na]$^+$		[dThd+Na]$^+$	
Conformer Designation	**T1(O2O4′O5′)**		**T1(O2O4′O5′)**	
Bond Length	Na^+···O2	2.185 Å	Na^+···O2	2.185 Å
	Na^+···O4′	2.416 Å	Na^+···O4′	2.416 Å
	Na^+···O5′	2.256 Å	Na^+···O5′	2.255 Å
Glycosidic Bond Length	N1···C1′	1.458 Å	N1···C1′	1.458 Å
Bond Angle	∠O2Na^+O4′	78.6°	∠O2Na^+O4′	78.6°
	∠O2Na^+O5′	136.5°	∠O2Na^+O5′	136.5°
	∠O4Na^+O5′	74.2°	∠O4Na^+O5′	74.2°
Dihedral Angle	∠C2N1C1′O4′	−61.6°	∠C2N1C1′O4′	61.6°
	∠O5′C5′C4′O4′	56.8°	∠O5′C5′C4′O4′	−56.8°

[a] Data for the D-enantiomers is taken from references [24] and [25].

4. Discussion

4.1. IRMPD and CID pathways

Energetic and structural characteristics of L-dThd precursor ions in this study were investigated using two fragmentation methods: IRMPD and ER-CID. Both of these fragmentation methods have proven to be reliable means for inducing dissociation among naturally-occurring and modified nucleosides [24,25,27–37] as well as other various biomolecules. Each of these techniques employed involves gradual excitation of the precursor ions to induce dissociation, but this is achieved using different activation mechanisms. The IRMPD mechanism employed in these experiments achieves ion dissociation through the absorption of multiple (tens to hundreds) infrared photons within a resonant vibrational mode of the precursor ion. With each IR photon absorbed, the precursor ion is promoted to an excited vibrational state until the absorbed energy is quickly dissipated to the bath of background vibrational states through intramolecular vibrational redistribution (IVR). Each subsequent infrared photon absorbed raises the internal energy of the ion until its dissociation threshold is exceeded, leading to precursor ion fragmentation [59]. When performing CID in a QIT MS, precursor ion dissociation is achieved by gradually increasing their internal energies through multiple energetic collisions with a neutral He buffer gas. The radiofrequency excitation voltage that is applied to the endcap electrodes of the ion trap accelerates the precursor ions to greater velocities and leads to greater kinetic-to-internal energy transfer per collision and thus the ion more rapidly achieves an internal energy that exceeds its dissociation threshold and induces fragmentation.

The fragmentation pathways observed for [L-dThd+H]$^+$, [L-dThd + Na]$^+$, [dThd+H]$^+$, and [dThd + Na]$^+$ with the IRMPD and ER-CID activation techniques exhibit parallel characteristics as well as distinct differences. As described earlier (Section 3.2), the IRMPD spectra demonstrate three photodissociation pathways (**Reactions 12–14**). As can be observed in Fig. 2, the CID mass spectra for both protonated and sodium cationized systems demonstrate eight different dissociation pathways (**Reactions 4–11**). Glycosidic bond cleavage is the dominant dissociation pathway observed for both IRMPD and CID excitation techniques (**Reactions 12** and **13** and **Reactions 4** and **5**, respectively). However, contrary to that observed with the IRMPD method, the CID excitation technique exhibits several dissociation pathways in addition to glycosidic bond cleavage and simple cation dissociation from the nucleoside. Competitive fragmentation pathways involving ketene and water losses (**Reactions 6** and **7**) are observed for both [L-dThd+H]$^+$ and [dThd+H]$^+$ systems along with minor dissociation pathways that contribute to the various ions observed in the protonated mass spectra (**Reactions 8–11**). The observation of these additional fragmentation pathways upon CID suggests more rapid heating/activation enabling slightly more energetic pathways to be accessed prior to dissociation. Simple dissociation of the Na^+ cation from the nucleoside occurs for both IRMPD and CID, but the *m/z* of Na^+ is below the low-mass cutoff of the QIT MS and is therefore not observed in the CID mass spectra of [L-dThd + Na]$^+$ and [dThd + Na]$^+$.

4.2. Experimental IRMPD enantiomer comparisons

After normalizing the raw IRMPD yields via the laser power calibration curves (see **Fig. S1**) to account for variations in the power output over the wavelength range investigated and applying scaling factors to account for different laser irradiation times in each of the systems investigated, the agreement between the protonated and sodium cationized spectra of L-dThd and dThd becomes more evident. Although IRMPD is a multiple photon process, the linear power corrections applied accurately represent the nonlinear experimental behavior and subsequent spectroscopic results that were observed. The experimental IRMPD spectra of [L-dThd+H]$^+$, [dThd+H]$^+$, [L-dThd + Na]$^+$, and [dThd + Na]$^+$ are compared in Fig. 4. In both the protonated and sodium cationized spectral comparisons, highly parallel results are observed for the L-dThd and dThd systems. These similarities are expected for enantiomers exhibit-

Table 2
Relative 0 K and 298 K Enthalpies and 298 K Gibbs Energies in kJ/mol, Pseudorotation Angles, Thymine Orientations, and Sugar Puckerings of Select Stable Low-Energy Conformers of $[L\text{-dThd+H}]^+$ and $[L\text{-dThd + Na}]^+$.[a]

Species	Conformer	Thymine Orientation	Sugar Puckering	ΔH_0	ΔH_{298}	ΔG_{298}	P (°)
$[L\text{-dThd+H}]^+$	**TA**	*anti*	C2′-endo ($^2T_3$)	0.1	1.5	0.0	166.0
	TB	*anti*	C3′-exo ($_3T^2$)	0.5	2.2	0.7	194.9
	TC	*syn*	C2′-endo ($^2T_1$)	0.0	0.0	3.0	151.6
	O4A	*anti*	C3′-exo ($_3T^2$)	4.0	6.1	3.3	192.5
	O4B	*anti*	C2′-endo ($^2T_3$)	5.6	7.7	3.8	166.9
	O2A	*syn*	C2′-endo ($^2T_1$)	1.4	1.6	4.2	153.2
	TD	*anti*	C2′-endo ($^2T_3$)	11.8	13.4	11.1	170.1
	TE	*anti*	C3′-exo ($_3T^4$)	12.9	14.5	13.0	198.1
	TF	*anti*	C2′-endo ($^2T_1$)	16.4	18.6	13.4	157.7
	TG	*anti*	C3′-exo ($_3T^2$)	14.5	16.5	13.8	195.6
	O4C	*anti*	C3′-exo ($_3T^4$)	15.7	17.7	15.3	201.1
	O4D	*anti*	C3′-exo ($_3T^2$)	16.2	18.6	15.3	166.9
	O4E	*anti*	C2′-endo ($^2T_3$)	17.4	19.6	15.4	168.8
	O4F	*anti*	C2′-endo ($^2T_3$)	18.3	20.6	16.2	213.3
	TH	*anti*	C3′-exo ($_3T^2$)	16.7	18.5	16.8	194.4
	TI	*anti*	C3′-exo ($_3T^4$)	23.4	26.1	18.0	208.0
	O4G	*anti*	C3′-exo ($_3T^4$)	23.2	25.5	20.3	192.0
	O4H	*anti*	C3′-exo ($_3T^4$)	20.8	22.9	20.5	200.5
	TJ	*anti*	C3′-exo ($_3T^4$)	22.1	23.9	22.0	224.5
	O2B	*syn*	C2′-endo ($^2T_3$)	23.4	24.2	23.2	169.8
$[L\text{-dThd + Na}]^+$	**T1(O2O4′O5′)**	*syn*	O4′-endo ($^OT_1$)	0.0	0.0	0.0	100.5
	T2(O2O4′O5′)	*syn*	C1′-exo ($_1T^O$)	5.0	5.3	4.6	108.3
	T3(O2O4′O5′)	*syn*	C2′-exo ($_2T^3$)	7.5	7.7	7.8	166.3
	T4(O2O4′O5′)	*syn*	C2′-endo ($^2T_1$)	9.4	9.9	8.4	148.5
	T5(O2O4′O5′)	*syn*	O4′-endo ($^OT_4$)	9.6	9.9	9.7	266.2
	T6(O2O4′O5′)	*syn*	C2′exo ($_2T^3$)	12.9	12.9	13.7	167.5
	T7(O2O4′O5′)	*syn*	O4′-endo ($^OT_1$)	15.9	16.4	15.4	98.5
	B1(O2O4′)	*syn*	C3′-exo ($_3T^2$)	32.1	32.8	30.1	192.5
	B1(O2O5′)	*syn*	C4′-exo ($_4T^3$)	31.9	32.4	31.6	224.4
	M1(O4)	*anti*	C2′-endo ($^2T_3$)	44.3	45.4	39.5	163.8
	B1(O2N3)	*anti*	C3′-exo ($_3T^2$)	48.8	50.4	45.6	195.9
	B1(O4′O5′)	*syn*	C3′-exo ($_3T^2$)	48.7	49.7	46.5	193.7
	B1(O3′O5′)	*syn*	C3′-exo ($_3T^2$)	48.2	48.5	46.8	189.5
	M1(O2)	*anti*	C2′-endo ($^2T_3$)	55.9	57.3	50.5	169.1
	B1(O2O3′)	*anti*	C2′-endo ($^2T_1$)	51.1	51.4	51.4	144.1
	B1(N3O4)	*syn*	C2′-endo ($^2T_1$)	53.2	52.9	53.8	147.4
	M1(O5′)	*syn*	C2′-endo ($^2T_3$)	76.9	76.8	73.6	178.4
	B1(O4O5′)	*anti*	C2′-endo ($^2T_3$)	75.9	75.3	78.3	167.3
	M1(O3′)	*syn*	C4′-endo ($^4T_3$)	97.1	97.9	91.8	219.1
	B1(O3′O4′)	*syn*	C3′-exo ($_3T^4$)	98.8	99.7	96.9	206.3

[a] Energetics based on single-point energy calculations performed at the B3LYP/6-311+G(2d,2p) level of theory, including ZPE and thermal corrections based on the B3LYP/6-311+G(d,p) optimized structures and vibrational frequencies.

ing simple cation binding. However, some variation is expected to occur in the experimental IRMPD results of these systems due to differences in the tuning parameters of the FT-ICR MS for each system, slight differences in the precursor ion *m/z* range selected in the SWIFT isolation used for each system, variations in the day-to-day tuning conditions of the FEL, other users simultaneously performing infrared experiments on different user stations in the FELIX facility (i.e., the operating frequency and beam intensity of the free electron laser (FEL) are slightly affected by these changes), and different users performing the experiments with a considerable span of time between the measurements for the L-dThd and dThd systems. Indeed, the original experiments for the protonated dThd systems were performed at the FOM Institute for Plasma Physics Rijnhuizen in 2012 [24]. However, the FELIX FEL was moved to its current location (at the Radboud University Nijmegen in 2013) where the measurements for the L-dThd systems were made last summer 2017, and the sodium cationized form of dThd was measured in 2016. Further, the geometry of the FEL was altered to fit into a somewhat smaller space. Combined, all of these factors might be expected to influence the measured IRMPD spectra.

IRMPD and theoretical studies of $[dThd+H]^+$ were previously reported by Wu and coworkers [24]. Fig. 4 illustrates the comparison between experimental IRMPD spectra of $[L\text{-dThd+H}]^+$ and $[dThd+H]^+$, where nearly all the features observed correspond primarily with the **TA** 2,4-dihydroxy tautomeric ground conformers with additional contributions from the **O2A** conformers in both L-dThd and dThd protonated systems, respectively. As expected for enantiomers exhibiting simple cation binding, both protonated spectra exhibit parallel behavior among major features observed. However, differences can still be seen in Fig. 4. These noticeable discrepancies observed in the peak positions and intensities in the fingerprint region are likely due to a combination of the effects discussed above.

The IRMPD and theoretical studies of $[dThd + Na]^+$ were previously reported by Zhu and coworkers [25]. Fig. 4 also shows the comparison between experimental IRMPD spectra of $[L\text{-dThd + Na}]^+$ and $[dThd + Na]^+$ where all major features have significant contributions from the respective **T1(O2O4′O5′)** ground conformers with some contributions from the respective **B1(O2O4′)** conformers. As can be readily observed, the sodium cationized spectra exhibit even more parallel features throughout the fingerprint and hydrogen-stretching regions. The high level of agreement between spectra may be due in large part to the similar experimental conditions employed between data collection and the spectra being acquired using the same instrument at the same facility compared to the protonated systems.

Table S1 compares the experimental IRMPD peak positions and relative yields of the features observed for the protonated

L-dThd and dThd systems. **Table S2** provides the same comparison for the sodium cationized L-dThd and dThd systems investigated. The largest difference in the measured vibrational frequency of the spectral features observed in both the protonated and sodium cationized spectra is 9 cm^{-1} with all analogous major peaks illustrating parallel characteristics. Eleven of the 13 spectral features observed for [L-dThd+H]$^+$ and 9 of the 13 features of [L-dThd + Na]$^+$ in the fingerprint region are blueshifted by 1–9 cm^{-1} compared to those observed for [dThd+H]$^+$ and [dThd + Na]$^+$. This may suggest a slight difference between wavelength calibrations applied to each system using the FEL excitation source because there is minimal spectral shifting in the hydrogen-stretching region between the protonated and sodium cationized systems where the OPO/OPA excitation source was employed.

Table S3 provides the vibrational frequency assignments corresponding to the theoretical IR and experimental IRMPD spectral features for [L-dThd+H]$^+$ and [L-dThd + Na]$^+$ along with the complementary dThd ions for comparison. The vibrational signatures of [L-dThd+H]$^+$ are primarily associated with the ground and dominant 2,4-dihydroxy tautomer, **TA**, with additional contributions from the low-energy **O2A** and **O4A** conformers. The vibrational signatures of [dThd+H]$^+$ also primarily arise from the ground and dominant 2,4-dihydroxy tautomer. **TA**, with additional contributions from the **O2A** conformer. The vibrational frequency assignments for both [L-dThd + Na]$^+$ and [dThd + Na]$^+$ are based on their respective ground **T1(O2O4′O5′)** conformers, and the experimental spectra illustrate highly parallel behavior among major bands observed as expected. Additional discussion of the vibrational frequency assignments for [L-dThd+H]$^+$ and [L-dThd + Na]$^+$ is available in the Supplementary material.

4.3. Comparison of experimental IRMPD and calculated IR spectra of [L-dThd+H]$^+$

Fig. 6 compares the experimental IRMPD spectrum of [L-dThd+H]$^+$ with the calculated IR spectra of several low-energy conformers (**TA**, **TB**, **TC**, **O4A**, and **O2A**). As can be seen in the figure, there is good agreement between each of the theoretical IR spectra and the measured IRMPD spectrum with several features unique to the 2,4-dihydroxy tautomers and others specific to the O2 and O4 protonated conformers. The bands observed at 1786 cm^{-1} and 3386 cm^{-1} are only associated with the **O2A** conformer, corresponding to the C4=O4 carbonyl stretch and N3–H stretch, whereas the band at 3582 cm^{-1} with its shoulder at 3567 cm^{-1} are only present with the T conformers, corresponding to the O2–H and O4–H combination stretches. The remaining features arise from both the T and O2 conformers in the fingerprint and hydrogen-stretching regions. The intense peak calculated at 1569 cm^{-1} of the **TC** conformer may contribute to the nonzero signal between the measured bands at 1598 cm^{-1} and 1529 cm^{-1}. However, clear disagreement is observed between the **O4A** calculated IR spectrum and the measured IRMPD spectrum. The strong feature calculated at 1569 cm^{-1} for **O4A** would likely broaden the immediately adjacent peaks at 1598 cm^{-1} and 1529 cm^{-1} or possibly contribute a redshifted shoulder feature to the observable 1598 cm^{-1} feature, but neither of these findings is observed indicating minimal **O4A** conformer population in the experiments. The predicted bands at 3600 cm^{-1} and 1293 cm^{-1} for **O4A** are also not observed in the measured IRMPD spectrum. However, the predicted feature at 1799 cm^{-1}, corresponding to the C2=O2 stretch, may slightly contribute to the blue shoulder of the carbonyl peak observed in the IRMPD spectrum. As a result, it can be reasonably concluded that **O4A** does not significantly contribute to the experimental ESI population.

In summary, the **TA**, **TB**, and **TC** 2,4-dihydroxy tautomers are populated in the ESI experiments with **TA** and **TB** theoretical spectra illustrating the closest agreement with the measured IRMPD spectrum and **TC** likely contributing to a lesser extent due to misalignment among major features with the IRMPD spectrum. **O2A** contributes to the experimental population and minor features observed in the experimental spectrum, but O4 protonated conformers of [L-dThd+H]$^+$ are likely minimally populated in the experiments. The predicted IR spectrum for a 3:3:1 mixture of the **TA**, **TB**, and **O2A** conformers, respectively, exhibits reasonable agreement with the measured IRMPD spectrum (see blue overlay in the top panel of Fig. 6) suggesting that the experimental population is comprised of ~86% 2,4-dihydroxy tautomers and ~14% O2 protonated conformers. These findings parallel results previously reported for [dThd+H]$^+$ [24].

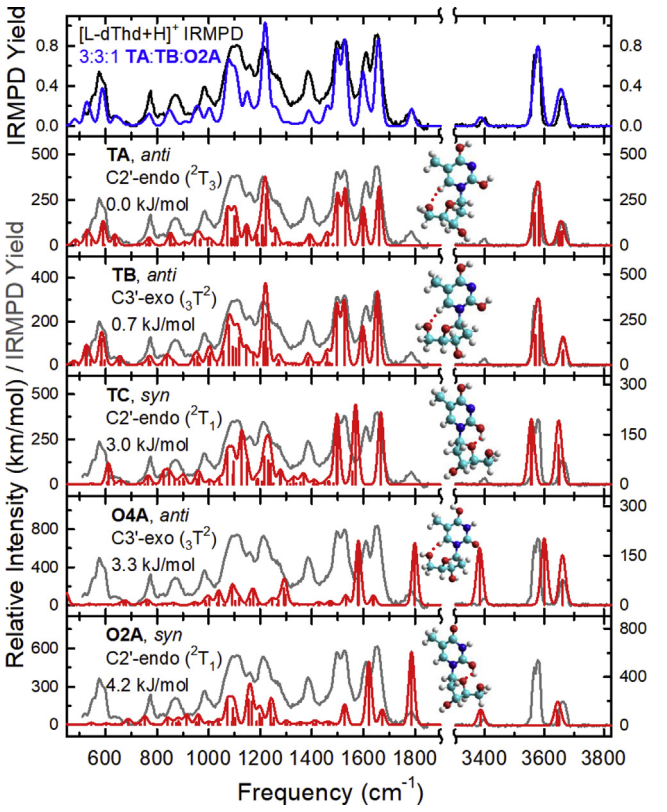

Fig. 6. Comparison of the experimental IRMPD action spectrum of [L-dThd+H]$^+$ with select low-energy B3LYP/6-311+G(d,p) optimized structures and their corresponding theoretical linear IR spectra. The site of protonation, tautomeric conformation, thymine orientation, sugar puckering, and B3LYP/6-311+G(2d,2p) relative Gibbs energies at 298 K are presented for each conformer. The IRMPD spectrum is overlaid in grey and scaled separately in the fingerprint and hydrogen-stretching regions to match the most intense peaks within the predicted IR spectra to facilitate comparisons of the observed features. The predicted IR spectrum for a 3:3:1 of the **TA**, **TB**, and **O2A** conformers, respectively, is overlaid in blue in the top panel (For interpretation of the references to colour in this figure legend, the reader is referred to the web version of this article).

4.4. Comparison of experimental IRMPD and calculated IR spectra of [L-dThd + Na]$^+$

Fig. 7 compares the experimental IRMPD spectrum of [L-dThd + Na]$^+$ with the calculated IR spectra of several low-energy conformers (**T1(O2O4′O5′)**, **T2(O2O4′O5′)**, **B1(O2O4′)**, **B1(O2O5′)**, and **M1(O4)**). The calculated IR spectra of the **T1(O2O4′O5′)**, **T2(O2O4′O5′)**, and **B1(O2O4′)** conformers exhibit the closest agreement with the experimental IRMPD spectrum. The tridentate conformers both have *syn* Thy nucleobase orientations but with different sugar puckerings, and their close agreement with the

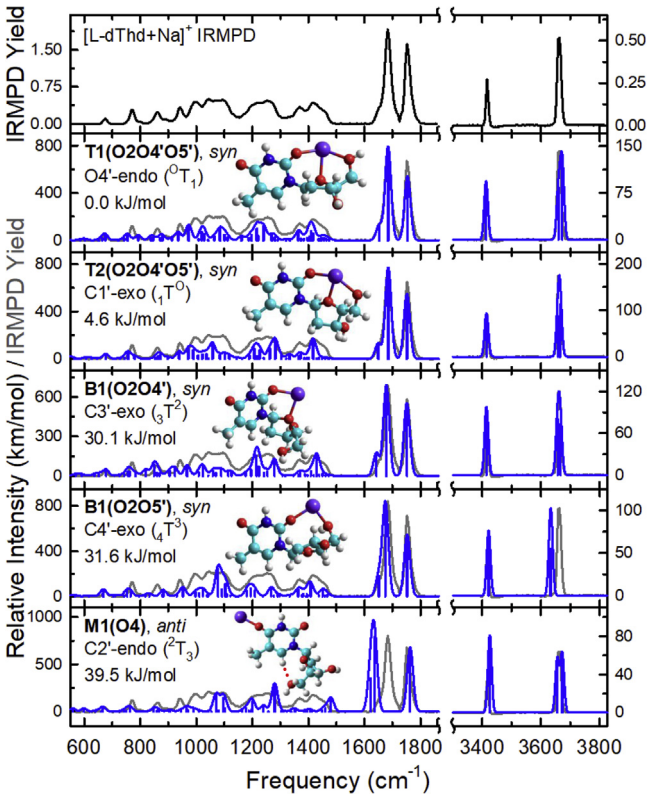

Fig. 7. Comparison of the experimental IRMPD action spectrum of [L-dThd + Na]$^+$ with select low-energy B3LYP/6-311+G(d,p) optimized structures and their corresponding theoretical linear IR spectra. The sodium cation binding mode, thymine orientation, sugar puckering, and B3LYP/6-311+G(2d,2p) relative Gibbs energies at 298 K are presented for each conformer. The IRMPD spectrum is overlaid in grey and scaled separately in the fingerprint and hydrogen-stretching regions to match the most intense peaks within the predicted IR spectra to facilitate comparisons of the observed features.

measured IMRPD spectrum indicates they are likely the dominant structures populated in the ESI experiments. Minor shifts in several computed bands are observed for the **B1(O2O4′)** conformer, including the shoulder at 1643 cm^{-1} shifted to the red compared to the experimental feature, and the band predicted at 1429 cm^{-1} is blueshifted compared to the measured IRMPD peak. The minor calculated features at 821 cm^{-1} and 919 cm^{-1} are also not easily discernible within the experimental IRMPD spectrum. Despite these minor discrepancies, the major computed bands for the **B1(O2O4′)** conformer align very well with the measured IRMPD spectrum, suggesting it may be populated in minor abundance in the experiments. However, its computed Gibbs energy, 30.1 kJ/mol relative to the ground **T1(O2O4′O5′)** conformer, suggest that its population is indeed expected to be quite small. The **B1(O2O5′)** conformer does not significantly contribute to the experimental population largely as the intense feature predicted at 3633 cm^{-1} is redshifted by 30 cm^{-1} compared to the experimental feature, and its high Gibbs energy, 31.6 kJ/mol versus the ground conformer reinforces its lack of importance. The **M1(O4)** conformer is not expected to be populated in the ESI experiments based on its high Gibbs energy, 39.5 kJ/mol; significant spectral mismatches are also observed including splitting of the feature at ~3663 cm^{-1} associated with the *anti* Thy nucleobase orientation and misalignments of the features predicted at 1632 cm^{-1} and 1480 cm^{-1} that do not align with the experimental spectrum.

In summary, the **T1(O2O4′O5′)** and **T2(O2O4′O5′)** conformers are dominantly populated in the ESI experiments. Spectral similarities suggest that the **B1(O2O4′)** conformer also makes very minor contributions. These findings parallel results previously reported for [dThd + Na]$^+$ [25].

4.5. Relative N-glycosidic bond stabilities

The survival yield curves of [L-dThd+H]$^+$, [L-dThd + Na]$^+$, [dThd+H]$^+$ and [dThd + Na]$^+$ are compared in Fig. 3. As can be seen in the figure, the L-dThd curves lie virtually on top of the dThd curves, an expected finding for enantiomers sharing the same physical properties. The ER-CID behavior of these systems were evaluated using the same method and experimental conditions to ensure meaningful comparisons among systems. The $CID_{50\%}$ values reported here for [dThd+H]$^+$ and [dThd + Na]$^+$ slightly differ from those previously reported due to minor differences in the ER-CID procedures employed [25]; however, the $CID_{50\%}$ values are the same within the reported margin of error. Multiple fragmentation pathways are observed for the protonated Thy nucleosides as described earlier (Section 3.1) involving a combination of neutral water and ketene losses, competing with the dominant glycosidic bond cleavage fragmentation pathway. Consequently, the $CID_{50\%}$ values reported for [L-dThd+H]$^+$ and [dThd+H]$^+$ do not directly correlate with glycosidic bond strength but rather the overall nucleoside stability. Compared to [L-dThd + Na]$^+$ and [dThd + Na]$^+$, protonation activates the glycosidic bond and sugar moiety more effectively at a lower rf_{EA} value, inducing a greater variety of fragmentation pathways beyond glycosidic bond cleavage. Among the sodium cationized Thy nucleosides, the dominant fragmentation pathway observed is glycosidic bond cleavage. As a result, the $CID_{50\%}$ values for [L-dThd + Na]$^+$ and [dThd + Na]$^+$ directly correlate with the relative glycosidic bond strengths.

The average N-glycosidic bond length predicted for [L-dThd+H]$^+$ is 1.522 Å; the O2 and O4 protonated structures exhibit slightly shorter average glycosidic bond lengths of 1.521 Å and 1.520 Å, respectively, whereas the T conformers have a slightly longer average glycosidic bond length of 1.525 Å. These results suggest that protonation induced tautomerization activates the glycosidic bond of L-dThd slightly more effectively than O2 and O4 protonation. The average N-glycosidic bond length predicted for the [L-dThd + Na]$^+$ complexes is 1.486 Å, indicating that sodium cationization is less effective at activating the glycosidic bond than protonation, consistent with the trends in the $CID_{50\%}$ values. The glycosidic bond lengths of each system are compared in **Table S4**. This behavior extends to the overall stabilities of the L-dThd nucleosides as well based upon the rf excitation amplitudes at $CID_{50\%}$ discussed earlier (Section 3.1). The rf_{EA} at $CID_{50\%}$ for [L-dThd + Na]$^+$ is nearly double the value of the rf_{EA} at $CID_{50\%}$ for [L-dThd+H]$^+$.

4.6. Robustness of the simulated annealing methodology

As described in Section 2.5, this study employed molecular dynamics simulated annealing procedures to generate candidate structures for higher level optimization for both the [L-dThd+H]$^+$ and [L-dThd + Na]$^+$ systems. This method samples energy accessible conformations for each of the systems in a random fashion while the structure is subjected to increasing and decreasing internal energy, allowing local and ideally global extrema to be accessed. Due to the limited number of possible protonation states, initial rounds of simulated annealing involving several manually-constructed structures did not sample the conformational space comprehensively enough to locate every low-energy conformer previously reported for [dThd+H]$^+$ [24]. To ensure comprehensive results, the mirror images of the dThd structures were generated for all 15 structures reported and were also subjected to the simulated annealing process. This procedure enabled all 15 conformers

to be found as their L-dThd enantiomers. This additional sampling also found more structures with a broader range of relative Gibbs energies, extending from the ground conformer to 76.0 kJ/mol. For the initial $[L\text{-dThd} + Na]^+$ structures, six different sites of Na^+ binding were examined in the first rounds of simulated annealing. These initial simulations produced 54 of the 80 previously reported $[dThd + Na]^+$ [25] structures. Thus again, enantiomeric conformers of $[dThd + Na]^+$ not found for $[L\text{-dThd} + Na]^+$ in the initial simulated annealing were subjected to stereochemical inversion, simulated annealing and higher level optimization such that the remaining 26 structures were also found. These results suggest that more comprehensive sampling is needed to avoid the need for manual intervention, but that combined very comprehensive sampling is achieved.

5. Conclusions

The IRMPD spectra of $[L\text{-dThd+H}]^+$ and $[L\text{-dThd} + Na]^+$ were acquired and compared with their respective theoretical linear IR spectra calculated at B3LYP/6-311+G(2d,2p)//B3LYP/6-311+G(d,p) level of theory to identify favorable states of protonation and sodium cationization among predicted low-energy conformers populated in the experiments and compared to previously reported findings involving their respective enantiomer $[dThd+H]^+$ [24] and $[dThd + Na]^+$ [25] ions. Gaussian 09 quantum chemical calculations identify the ground conformer of $[L\text{-dThd+H}]^+$ demonstrating a 2,4-dihydroxy tautomeric protonation state with an *anti* Thy nucleobase orientation and C2′-endo ($^2T_3$) sugar puckering, the exact enantiomer of the ground conformer reported for $[dThd+H]^+$ [24]. Theory predicts low-energy 2,4-dihydroxy tautomers with an *anti* nucleobase orientation as the dominant species in the experimental ESI population with minor contributions from O2 protonated conformers and possible trace contributions from O4 protonated conformers. DFT calculations predicted that the ground conformer of $[L\text{-dThd} + Na]^+$ exhibits tridentate coordination of the sodium cation by the nucleobase O2 and sugar O4′ and O5′ atoms with a *syn* nucleobase orientation and O4′-endo ($^OT_1$) sugar puckering. This is, again, the exact enantiomer of the ground conformer reported for $[dThd + Na]^+$ [25]. Theory predicts low-energy tridentate conformers involving Na^+ binding with O2, O4′, and O5′ atoms adopting a *syn* nucleobase orientation as the dominant species populated in the ESI experiments with additional minor contributions from O2O4′ bidentate species and no contribution from monodentate species. The high level of agreement between the calculated linear IR spectra and experimental IRMPD spectra among the low-energy conformers illustrates the validity of these predictions as well as the enantiomeric species, for both $[L\text{-dThd+H}]^+$ and $[L\text{-dThd} + Na]^+$ as well as $[dThd+H]^+$ and $[dThd + Na]^+$ [24,25]. The overall stability and N-glycosidic bond stability of $[L\text{-dThd} + Na]^+$ exceeds that of $[L\text{-dThd+H}]^+$ as also observed for $[dThd + Na]^+$ and $[dThd+H]^+$, indicating that sodium cationization activates the glycosidic bond less effectively than protonation for both L-dThd and dThd. The theoretical and experimental results for $[L\text{-dThd+H}]^+$ and $[L\text{-dThd} + Na]^+$ exhibit nearly identical behavior to that found previously for $[dThd+H]^+$ [24] and $[dThd + Na]^+$ [25], indicating a clear parallel as expected among enantiomers using the robust methodology employed in this study.

The highly parallel results of this L-dThd study observed with the previously reported findings for dThd [24,25] further validate the theoretical and experimental techniques utilized in this work. Despite different laser setups being employed for the protonated and sodium cationized D-thymidine and L-thymidine systems located at different facilities over an approximate five year time span, this study substantiates the same theoretical and experimental results as expected for respective enantiomer systems exhibiting simple cation binding.

Funding

This work was financially supported by the National Science Foundation, grants OISE-1357887 (for the IRMPD measurements and international travelling costs), DBI-0922819 (for the Bruker amaZon ETD QIT MS employed in this work), and CHE1709789 (for other research costs). Z.J.D. and L.A.H. gratefully acknowledge support from the WSU Thomas C. Rumble Fellowship. Z.J.D. gratefully acknowledges additional support from the WSU Joseph Jasper Scholarship for Graduate Students in Chemistry.

Acknowledgements

The authors thank Wayne State University Computing & Information Technology for computational resources and support. The authors are grateful to the Nederlandse Organisatie voor Wetenschappelijk Onderzoek (NWO) for financial support of the FELIX Laboratory. The skillful assistance of the FELIX staff is gratefully acknowledged.

Appendix A. Supplementary data

Supplementary material related to this article can be found, in the online version, at doi:https://doi.org/10.1016/j.ijms.2019.04.003.

References

[1] P.E. Boehmer, I.R. Lehman, Herpes simplex virus DNA replication, Annu. Rev. Biochem. 66 (1997) 347–384, http://dx.doi.org/10.1146/annurev.biochem.66.1.347.
[2] A. Telesnitsky, S.P. Goff, Reverse transcriptase and the generation of retroviral DNA, in: J.M. Coffin, S.H. Hughes, H.E. Varmus (Eds.), Retroviruses, Cold Spring Harbor, Cold Spring Harbor Laboratory Press, New York, 1997, available at https://www.ncbi.nlm.nih.gov/books/NBK19383/.
[3] W.M. Lee, Hepatitis B virus infection, N. Engl. J. Med. 337 (1997) 1733–1745, http://dx.doi.org/10.1056/nejm199712113372406.
[4] T.J. Liang, Hepatitis B: the virus and disease, Hepatology 49 (2009) S13–S21, http://dx.doi.org/10.1002/hep.22881.
[5] S.J. Matthews, Telbivudine for the management of chronic hepatitis B virus infection, Clin. Ther. 29 (2007) 2635–2653, http://dx.doi.org/10.1016/j.clinthera.2007.12.032.
[6] D.N. Amarapurkar, Telbivudine: a new treatment for chronic hepatitis B, World J. Gastroenterol. 13 (2007) 6150–6155, http://dx.doi.org/10.3748/wjg.v13.i46.6150.
[7] Global Hepatitis Report, World Health Organization, Geneva, 2017, https://www.who.int/hepatitis/publications/global-hepatitis-report2017/en/.
[8] C. Mathe, G. Gosselin, L-nucleoside enantiomers as antiviral drugs: a mini-review, Antiviral Res. 71 (2006) 276–281, http://dx.doi.org/10.1016/j.antiviral.2006.04.017.
[9] A. Alberti, N. Caporaso, HBV therapy: guidelines and open issues, Dig. Liver Dis. 43S (2011) S57–S63, http://dx.doi.org/10.1016/S1590-8658(10)60693-7.
[10] E.H. Buster, K.J. van Erpecum, S.W. Schalm, H.L. Zaaijer, J.T. Brouwer, H.C. Gelderblom, R.J. de Knegt, C. Minke Bakker, H.W. Reesink, H.L. Janssen, Treatment of chronic hepatitis B virus infection - Dutch national guidelines, Neth. J. Med. 66 (2008) 292–306, http://www.njmonline.nl/getpdf.php?id=692.
[11] Y.F. Liaw, Natural history of chronic hepatitis B virus infection and long-term outcome under treatment, Liver Int. 29 (2009) 100–107, http://dx.doi.org/10.1111/j.1478-3231.2008.01941.x.
[12] E.D. Clercq, The design of drugs for HIV and HCV, Nat. Rev. Drug Discov. 6 (2007) 1001, http://dx.doi.org/10.1038/nrd2424.
[13] E.D. Clercq, Anti-HIV drugs: 25 compounds approved within 25 years after the discovery of HIV, Int. J. Antimicrob. Agents 33 (2009) 307–320, http://dx.doi.org/10.1016/j.ijantimicag.2008.10.010.
[14] K.K. Biron, Antiviral drugs for cytomegalovirus diseases, Antiviral Res. 71 (2006) 154–163, http://dx.doi.org/10.1016/j.antiviral.2006.05.002.
[15] J. Zhang, F. Visser, K.M. King, S.A. Baldwin, J.D. Young, C.E. Cass, The role of nucleoside transporters in cancer chemotherapy with nucleoside drugs, Cancer Metastasis Rev. 26 (2007) 85–110, http://dx.doi.org/10.1007/s10555-007-9044-4.
[16] F. Focher, S. Spadari, G. Maga, Antivirals at the mirror: the lack of stereospecificity of some viral and human enzymes offers novel opportunities

in antiviral drug development, Infect. Disord. Drug Targets 3 (2003) 41–53, http://dx.doi.org/10.2174/1568005033342163.
[17] E.D. Clercq, G. Li, Approved antiviral drugs over the past 50 years, Clin. Microbiol. Rev. 29 (2016) 695–747, http://dx.doi.org/10.1128/CMR.00102-15.
[18] C.-L. Lai, E. Gane, Y.-F. Liaw, C.-W. Hsu, S. Thongsawat, Y. Wang, Y. Chen, E.J. Heathcote, J. Rasenack, N. Bzowej, N.V. Naoumov, A.M. Di Bisceglie, S. Zeuzem, Y.M. Moon, Z. Goodman, G. Chao, B.F. Constance, N.A. Brown, Telbivudine versus lamivudine in patients with chronic hepatitis B, N. Engl. J. Med. 357 (2007) 2576–2588, http://dx.doi.org/10.1056/NEJMoa066422.
[19] J. Hou, Y.K. Yin, D. Xu, D. Tan, J. Niu, X. Zhou, Y. Wang, L. Zhu, Y. He, H. Ren, M. Wan, C. Chen, S. Wu, Y. Chen, J. Xu, Q. Wang, L. Wei, G. Chao, B.F. Constance, G. Harb, N.A. Brown, J. Jia, Telbivudine versus lamivudine in chinese patients with chronic hepatitis B: results at 1 year of a randomized, double-blind trial, Hepatology 47 (2008) 447–454, http://dx.doi.org/10.1002/hep.22075.
[20] C.-L. Lai, N. Leung, E.-K. Teo, M. Tong, F. Wong, H.-W. Hann, S. Han, T. Poynard, M. Myers, G. Chao, D. Lloyd, N.A. Brown, A 1-Year trial of Telbivudine, lamivudine, and the combination in patients with hepatitis B e antigen—positive chronic hepatitis B, Gastroenterology 129 (2005) 528–536, http://dx.doi.org/10.1053/j.gastro.2005.05.053.
[21] Y.F. Liaw, E. Gane, N. Leung, S. Zeuzem, Y. Wang, C.L. Lai, E.J. Heathcote, M. Manns, N. Bzowej, J. Niu, S.H. Han, S.G. Hwang, Y. Cakaloglu, M.J. Tong, G. Papatheodoridis, Y. Chen, N.A. Brown, E. Albanis, K. Galil, N.V. Naoumov, 2-year GLOBE trial results: telbivudine is superior to lamivudine in patients with chronic hepatitis B, Gastroenterology 136 (2009) 486–495, http://dx.doi.org/10.1053/j.gastro.2008.10.026.
[22] G.-R. Han, M.-K. Cao, W. Zhao, H.-X. Jiang, C.-M. Wang, S.-F. Bai, X. Yue, G.-J. Wang, X. Tang, Z.-X. Fang, A prospective and open-label study for the efficacy and safety of Telbivudine in pregnancy for the prevention of perinatal transmission of hepatitis B virus infection, J. Hepatol. 55 (2011) 1215–1221, http://dx.doi.org/10.1016/j.jhep.2011.02.032.
[23] J. Liang, M.J. Jiang, X. Deng, X. Xiao Zhou, Efficacy and safety of telbivudine compared to entecavir among HBeAg+ chronic hepatitis B patients: a meta-analysis study, Hepat. Mon. 13 (2013), e7862, http://dx.doi.org/10.5812/hepatmon.7862.
[24] R.R. Wu, B. Yang, C.E. Frieler, G. Berden, J. Oomens, M.T. Rodgers, 2,4-Dihydroxy and O2 protonated tautomers of dThd and thd coexist in the gas phase: methylation alters protonation preferences versus dUrd and Urd, J. Am. Soc. Mass Spectrom. 27 (2016) 410–421, http://dx.doi.org/10.1007/s13361-015-1303-y.
[25] Y. Zhu, H.A. Roy, N.A. Cunningham, S.F. Strobehn, J. Gao, M.U. Munshi, G. Berden, J. Oomens, M.T. Rodgers, IRMPD action spectroscopy, ER-CID experiments, and theoretical studies of sodium cationized thymidine and 5-methyluridine: kinetic trapping during the ESI desolvation process preserves the solution structure of $[Thd+Na]^+$, J. Am. Soc. Mass Spectrom. 28 (2017) 2423–2437, http://dx.doi.org/10.1007/s13361-017-1753-5.
[26] J.Y. Salpin, D. Scuderi, Structure of protonated thymidine characterized by infrared multiple photon dissociation and quantum calculations, Rapid Commun. Mass Spectrom. 29 (2015) 1898–1904, http://dx.doi.org/10.1002/rcm.7296.
[27] R.R. Wu, B. Yang, G. Berden, J. Oomens, M.T. Rodgers, Gas-phase conformations and energetics of protonated 2′-deoxyadenosine and adenosine: IRMPD action spectroscopy and theoretical studies, J. Phys. Chem. B 119 (2015) 2795–2805, http://dx.doi.org/10.1021/jp509267k.
[28] R.R. Wu, B. Yang, C.E. Frieler, G. Berden, J. Oomens, M.T. Rodgers, N3 and O2 protonated tautomeric conformations of 2′-deoxycytidine and cytidine coexist in the gas phase, J. Phys. Chem. B 119 (2015) 5773–5784, http://dx.doi.org/10.1021/jp5130316.
[29] R.R. Wu, B. Yang, G. Berden, J. Oomens, M.T. Rodgers, Gas-phase conformations and energetics of protonated 2′-deoxyguanosine and guanosine: IRMPD action spectroscopy and theoretical studies, J. Phys. Chem. B 118 (2014) 14774–14784, http://dx.doi.org/10.1021/jp508019a.
[30] R.R. Wu, B. Yang, C.E. Frieler, G. Berden, J. Oomens, M.T. Rodgers, Diverse mixtures of 2,4-dihydroxy tautomers and O4 protonated conformers of uridine and 2′-deoxyuridine coexist in the gas phase, Phys. Chem. Chem. Phys. 17 (2015) 25978–25988, http://dx.doi.org/10.1039/c5cp02227d.
[31] Y. Zhu, L.A. Hamlow, C.C. He, S.F. Strobehn, J.K. Lee, J. Gao, G. Berden, J. Oomens, M.T. Rodgers, Influence of sodium cationization versus protonation on the gas-phase conformations and glycosidic bond stabilities of 2′-deoxyadenosine and adenosine, J. Phys. Chem. B 120 (2016) 8892–8904, http://dx.doi.org/10.1021/acs.jpcb.6b06105.
[32] Y. Zhu, L.A. Hamlow, C.C. He, H.A. Roy, N.A. Cunningham, M.U. Munshi, G. Berden, J. Oomens, M.T. Rodgers, Conformations and N-glycosidic bond stabilities of sodium cationized 2′-deoxycytidine and cytidine: solution conformation of $[Cyd+Na]^+$ is preserved upon ESI, Int. J. Mass Spectrom. 429 (2018) 18–27, http://dx.doi.org/10.1016/j.ijms.2017.04.005.
[33] Y. Zhu, L.A. Hamlow, C.C. He, J.K. Lee, J. Gao, G. Berden, J. Oomens, M.T. Rodgers, Gas-phase conformations and N-glycosidic bond stabilities of sodium cationized 2′-deoxyguanosine and guanosine: sodium cations preferentially bind to the guanine residue, J. Phys. Chem. B 121 (2017) 4048–4060, http://dx.doi.org/10.1021/acs.jpcb.7b02906.
[34] Y. Zhu, H.A. Roy, N.A. Cunningham, S.F. Strobehn, J. Gao, M.U. Munshi, G. Berden, J. Oomens, M.T. Rodgers, Effects of sodium cationization *versus* protonation on the conformations and *N*-glycosidic bond stabilities of sodium cationized urd and dUrd: solution conformation of $[Urd+Na]^+$ is preserved upon ESI, Phys. Chem. Chem. Phys. 19 (2017) 17637–17652, http://dx.doi.org/10.1039/C7CP02377D.
[35] Z.J. Devereaux, Y. Zhu, M.T. Rodgers, Relative glycosidic bond stabilities of naturally-occurring methylguanosines: 7-methylation is intrinsically activating, Eur. J. Mass Spectrom. 25 (2019) 10–22, http://dx.doi.org/10.1177/1469066718798097.
[36] C.C. He, L.A. Hamlow, Z.J. Devereaux, Y. Zhu, Y.-w. Nei, L. Fan, C.P. McNary, P. Maitre, V. Steinmetz, B. Schindler, I. Compagnon, P.B. Armentrout, M.T. Rodgers, Structural and energetic effects of O2′-ribose methylation of protonated purine nucleosides, J. Phys. Chem. B 122 (2018) 9147–9160, http://dx.doi.org/10.1021/acs.jpcb.8b07687.
[37] L.A. Hamlow, Y. Zhu, Z.J. Devereaux, N.A. Cunningham, G. Berden, J. Oomens, M.T. Rodgers, Modified quadrupole ion trap mass spectrometer for infrared ion spectroscopy: application to protonated thiated uridines, J. Am. Soc. Mass Spectrom. 29 (2018) 2125–2137, http://dx.doi.org/10.1007/s13361-018-2047-2.
[38] H.U. Ung, K.T. Huynh, J.C. Poutsma, J. Oomens, G. Berden, T.H. Morton, Investigation of proton affinities and gas phase vibrational spectra of protonated nucleosides, deoxynucleosides, and their analogs, Int. J. Mass Spectrom. 378 (2015) 294–302, http://dx.doi.org/10.1016/j.ijms.2014.09.017.
[39] L. Feketeová, B. Chan, G.N. Khairallah, V. Steinmetz, P. Maître, L. Radom, A. Richard, Gas-phase structure and reactivity of the keto tautomer of the deoxyguanosine radical cation, Phys. Chem. Chem. Phys. 17 (2015) 25837–25844, http://dx.doi.org/10.1039/C5CP01573A.
[40] A. Filippi, C. Fraschetti, F. Rondino, S. Piccirillo, V. Steinmetz, L. Guidoni, M. Speranza, Protonated pyrimidine nucleosides probed by IRMPD spectroscopy, Int. J. Mass Spectrom. 354 (2013) 54–61, http://dx.doi.org/10.1016/j.ijms.2013.05.016.
[41] F.L. Bazsó, O. Ozohanics, G. Schlosser, K. Ludányi, K. Vékey, L. Drahos, Quantitative comparison of tandem mass spectra obtained on various instruments, J. Am. Soc. Mass Spectrom. 27 (2016) 1357–1365, http://dx.doi.org/10.1007/s13361-016-1408-y.
[42] A. Memboeuf, A. Nasioudis, S. Indelicato, F. Pollreisz, A. Kuki, S. Keki, O.Fvd. Brink, K. Vekey, L. Drahos, Size effect on fragmentation in tandem mass spectrometry, Anal. Chem. 82 (2010) 2294–2302, http://dx.doi.org/10.1021/ac902463q.
[43] A. Kuki, L. Nagy, A. Memboeuf, L. Drahos, K. Vékey, M. Zsuga, S. Kéki, Energy-dependent collision-induced dissociation of lithiated polytetrahydrofuran: effect of the size on the fragmentation properties, J. Am. Soc. Mass Spectrom. 21 (2010) 1753–1761, http://dx.doi.org/10.1016/j.jasms.2010.06.013.
[44] T.M. Kertesz, L.H. Hall, D.W. Hill, D.F. Grant, CE50: quantifying collision induced dissociation energy for small molecule characterization and identification, J. Am. Soc. Mass Spectrom. 20 (2009) 1759–1767, http://dx.doi.org/10.1016/j.jasms.2009.06.002.
[45] X. Guo, M.C. Duursma, P.G. Kistemaker, N.M.M. Nibbering, K. Vekey, L. Drahos, R.M.A. Heeren, Manipulating internal energy of protonated biomolecules in electrospray ionization fourier transform ion cyclotron resonance mass spectrometry, J. Mass Spectrom. 38 (2003) 597–606, http://dx.doi.org/10.1002/jms.480.
[46] K. Vékey, Internal energy effects in mass spectrometry, J. Mass Spectrom. 31 (1996) 445–463, http://dx.doi.org/10.1002/(SICI)1096-9888(199605)31:5<445::AID-JMS354>3.0.CO;2-G.
[47] K.J. Hart, S.A. McLuckey, Relative dissociation energy measurements using ion trap collisional activation, J. Am. Soc. Mass Spectrom. 5 (1994) 250–259, http://dx.doi.org/10.1016/1044-0305(94)85015-1.
[48] F. Derwa, Ed. Pauw, P. Natalis, New basis for a method for the estimation of secondary ion internal energy distribution in 'Soft' ionization techniques, J. Mass Spectrom. 26 (1991) 117–118, http://dx.doi.org/10.1002/oms.1210260215.
[49] D. Oepts, A.F.Gvd. Meer, P.Wv. Amersfoort, The free-electron-laser user facility FELIX, Infrared Phys. Technol. 36 (1995) 297–308, http://dx.doi.org/10.1016/1350-4495(94)00074-U.
[50] N.C. Polfer, J. Oomens, D.T. Moore, Gv. Helden, G. Meijer, R.C. Dunbar, Infrared spectroscopy of phenylalanine Ag(I) and Zn(II) complexes in the gas phase, J. Am. Chem. Soc. 128 (2006) 517–525, http://dx.doi.org/10.1021/ja0549291.
[51] N.C. Polfer, J. Oomens, Reaction products in mass spectrometry elucidated with infrared spectroscopy, Phys. Chem. Chem. Phys. 9 (2007) 3804–3817, http://dx.doi.org/10.1039/b702993b.
[52] J.J. Valle, J.R. Eyler, J. Oomens, D.T. Moore, A.F.Gvd. Meer, Gv. Helden, G. Meijer, C.L. Hendrickson, A.G. Marshall, G.T. Blakney, Free electron laser-fourier transform ion cyclotron resonance mass spectrometry facility for obtaining infrared multiphoton dissociation spectra of gaseous ions, Rev. Sci. Instrum. 76 (2005) 023103–023107, http://dx.doi.org/10.1063/1.1841953.
[53] K. Wolinski, J.F. Hinton, D.S. Wishart, B.D. Sykes, F.M. Richards, A. Pastone, V. Saudek, P.D. Ellis, G.E. Maciel, J.W. McIver, A.C. Blizzard, D.P. Santry, J.A. Pople, N.S. Ostlund, L. Ducasse, J. Hoarau, M. Pesquer, M. Kondo, I. Ando, R. Chujo, A. Nishioka, E.C. Vauthier, S. Odiot, F. Tonnard, J.D. Baker, M.C. Zerner, D.V. Beveridge, W.P. Anderson, T.R. Cundari, R.C. Bingham, M.J.S. Dewar, D.H. Lo, J. Li, P.C. Mello, K. Jug, W. Tihiel, E.G. Zoebisch, E.F. Healy, J.J.P. Stewart, M. Fraser, D.M. Hayes, HyperChem Computational Chemistry Software Package, 8.0.10, Hypercube, Inc., Gainesville, FL, 2004.
[54] M.J. Frisch, G.W. Trucks, H.B. Schlegel, G.E. Scuseria, M.A. Robb, J.R. Cheeseman, G. Scalmani, V. Barone, B. Mennucci, G.A. Petersson, H. Nakatsuji, M. Caricato, X. Li, H.P. Hratchian, A.F. Izmaylov, J. Bloino, G. Zheng, J.L. Sonnenberg, M. Hada, M. Ehara, K. Toyota, R. Fukuda, J. Hasegawa, M. Ishida, T. Nakajima, Y. Honda, O. Kitao, H. Nakai, T. Vreven, J. Montgomery, J. A, J.E. Peralta, F. Ogliaro, M.J. Bearpark, J. Heyd, E.N. Brothers, K.N. Kudin, V.N.

Staroverov, R. Kobayashi, J. Normand, K. Raghavachari, A.P. Rendell, J.C. Burant, S.S. Iyengar, J. Tomasi, M. Cossi, N. Rega, N.J. Millam, M. Klene, J.E. Knox, J.B. Cross, V. Bakken, C. Adamo, J. Jaramillo, R. Gomperts, R.E. Stratmann, O. Yazyev, A.J. Austin, R. Cammi, C. Pomelli, J.W. Ochterski, R.L. Martin, K. Morokuma, V.G. Zakrzewski, G.A. Voth, P. Salvador, J.J. Dannenberg, S. Dapprich, A.D. Daniels, O. Farkas, J.B. Foresman, J.V. Ortiz, J. Cioslowski, D.J. Fox, Gaussian 09, Revision A.02, Gaussian Inc., Pittsburgh, PA, 2009.

[55] J.P. Merrick, D. Moran, L. Radom, An evaluation of harmonic vibrational frequency scale factors, J. Phys. Chem. A 111 (2007) 11683–11700, http://dx.doi.org/10.1021/jp073974n.

[56] R.R. Wu, M.T. Rodgers, Tautomerization lowers the activation barriers for N-glycosidic bond cleavage of protonated uridine and 2′-deoxyuridine, Phys. Chem. Chem. Phys. 18 (2016) 24451–24459, http://dx.doi.org/10.1039/C6CP03620A.

[57] R.R. Wu, M.T. Rodgers, O2 protonation controls threshold behavior for N-glycosidic bond cleavage of protonated cytosine nucleosides, J. Phys. Chem. B 120 (2016) 4803–4811, http://dx.doi.org/10.1021/acs.jpcb.6b04388.

[58] W. Saenger, Principles of Nucleic-Acid Structure, Springer-Verlag, New York, 1984, pp. 16–104.

[59] N.C. Polfer, Infrared multiple photon dissociation spectroscopy of trapped ions, Chem. Soc. Rev. 40 (2011) 2211–2221, http://dx.doi.org/10.1039/c0cs00171f.